Results in Physics 39 (2022) 105689

Contents lists available at ScienceDirect

Results in Physics

journal homepage: www.elsevier.com/locate/rinp

Greenish-yellow emission from rare-earth free Li^+ doped zinc vanadate phosphor

Vaibhav Chauhan [a], Pratik Deshmukh [b], S. Satapathy [b], Praveen C. Pandey [a,*]

[a] Department of Physics, Indian Institute of Technology (Banaras Hindu University), Varanasi 221005, U.P., India
[b] Functional Bio-Materials Lab., Laser Biomedical Applications Division, Raja Ramanna Centre for Advanced Technology, Indore 452013, India

ARTICLE INFO

Keywords:
Zinc vanadate
Rare-earth free phosphors
Thermal stability
Li^+ ion
Photoluminescence

ABSTRACT

In this article, we present synthesis and spectral study of $Zn_{(3-x)}Li_x(VO_4)_2$ (x = 0, 0.01, 0.02, 0.03) samples. The orthorhombic phase of all the samples is validated by their XRD pattern. The crystallinity of $Zn_3(VO_4)_2$ is improved by doping Li^+ ions and is supported by the augmentation in crystallite size. The absorption band of the phosphors covers the near-UV region. The XPS analysis ascertains the V^{+5} oxidation state of vanadium thereby confirming the single-phase of the phosphors. The Li^+ ion doping enhances the broadband excitation in the near UV region and emission band of $Zn_3(VO_4)_2$ in the visible region with stokes shift of 9517.3 cm^{-1}. The increased PL lifetime of the emission bands is observed after Li^+ ion doping. The calculated activation energy of Li^+ doped $Zn_3(VO_4)_2$ phosphor is 0.29 eV and there is a 44% loss of emission intensity at 150 °C. Thus, with the broadband near-UV excitation and greenish-yellow emission, the Li^+ doped zinc vanadate phosphor can be utilized with near-UV LED chips for the realization of white light.

Introduction

White light-emitting diodes (wLEDs) have received a lot of attention recently in the field of solid-state lighting industry because of their significant advantages such as high luminous efficacy, eco-friendliness, enhanced optical power, longer operational lifetime, and energy efficacy [1]. The commercial wLEDs are fabricated by coating Ce^{3+}:YAG yellow phosphor over the blue chips [2,3]. However, such white light lacks sufficient distribution of power in the red region of visible spectrum which results in high correlated color temperature (CCT > 4500 K) and poor color rendering index (CRI < 75) [4]. To address this issue, researchers have proposed several rare-earth-doped single host materials for wLED application [5-8]. But the approaches for high-cost refining, separation, and purification of all the rare-earth materials make them expensive [9]. Therefore, there is a need to develop rare-earth-free self-luminescent phosphors for lighting and other optoelectronic applications. In this regard, materials such as vanadate and tungstate have been studied for their use in the solid-state lighting.

Vanadate compounds are potential materials for application in the fields of electrochemistry, solid-state lighting devices, catalysis, and optical lasers [10-15]. The findings of yttrium vanadate prompted the synthesis and study of many vanadate phosphors for their self-luminescence property [16]. The self-luminescence property of vanadate compounds has made them advantageous over commercial rare-earth-activated phosphors. The emission spectra of many vanadate compounds cover the full visible range and also have near Ultraviolet (UV) excitation [17-19]. The near UV absorption of vanadate phosphors overlaps the emission spectrum of the commercially available near UV LED chips used in wLED fabrication and therefore vanadate phosphors can be is used with near UV chips for the realization of white light [18,20]. The luminescence of vanadate compounds is owed to their VO_4 tetrahedral with T_d symmetry [17]. In VO_4 tetrahedral, the charge transfer from 2p orbitals of O^{2-} to 3d orbitals of V^{5+} takes place, thereby yielding a broadband emission spectrum that covers the whole visible range [21]. Thus, this self-luminescence property along with a low-cost synthesis process and energy efficiency adds to the advantage of vanadate phosphors over conventional phosphors [17-19].

Among different vanadate phosphors, zinc vanadate ($Zn_3(VO_4)_2$) phosphor has been explored as an effective solar energy transfer material, photo-catalyst, and white light-emitting phosphor [10-12]. Nakajima et al. have widely investigated the $M_3V_2O_8$ (M = Zn, Ba, Sr, and Ca) material system and the correlation between the structural properties and Quantum efficiency (QE) of $M_3V_2O_8$ vanadates with isolated VO_4 tetrahedra [22-24]. They concluded that the weak interaction between

* Corresponding author.
E-mail address: pcpandey.app@iitbhu.ac.in (P.C. Pandey).

https://doi.org/10.1016/j.rinp.2022.105689
Received 24 March 2022; Received in revised form 18 May 2022; Accepted 2 June 2022
Available online 3 June 2022

V^{5+} and M^{2+} ions and the strong interaction between the V ions in the $M_3V_2O_8$ crystal system strongly influence the QE of these phosphors. Their findings reveal that the $Zn_3(VO_4)_2$ phosphor has the highest emission and QE compared to other $M_3V_2O_8$ (M = Sr, Ba, and Ca) phosphors. Moreover, the QE of $Zn_3(VO_4)_2$ is also more than many reported garnet vanadate phosphors [25]. Thus, the choice of $Zn_3(VO_4)_2$ over other $M_3V_2O_8$ (M = Sr, Ba, and Ca) phosphors is clear.

There are few reports on the single-phase $Zn_3(VO_4)_2$ phosphor. This is because vanadium has multiple oxidation states and $Zn_3(VO_4)_2$ is sensitive to the synthesis process and annealing temperature. Previous reports on $Zn_3(VO_4)_2$ phosphor conclude that an additional monoclinic phase ($Zn_2V_2O_7$) is formed along with the primary orthorhombic phase [10,26–29]. Nakajima et al. have published a synthesis of $Zn_3(VO_4)_2$ by the high-temperature solid-state method [22,23]. Shibing et al. have reported the synthesis of $Zn_3(VO_4)_2$ microparticles, which require 10 h annealing in the N_2 atmosphere [30]. Therefore, there is a need to synthesize single-phase $Zn_3(VO_4)_2$ phosphor by the energy-efficient method. Herein, we report a facile citrate sol–gel method for the synthesis of single-phase $Zn_{(3-x)}Li_x(VO_4)_2$ (x = 0, 0.01, 0.02, 0.03) phosphors, where the dried gel was annealed at 700 °C for 4 h. With low annealing temperature and less annealing time, our synthesis technique is energy efficient as compared to earlier reported techniques. Moreover, in the sol–gel method, the reagents are mixed homogenously in an aqueous solution. The single phase of prepared phosphors is validated by the Rietveld refinement of the x-ray diffraction (XRD) data and is supported by Fourier transform infrared (FTIR) spectroscopy analysis. Moreover, the V^{5+} oxidation state of the vanadium is validated by X-ray photoelectron spectroscopy (XPS).

The influence of Li^+ ion on the luminescence properties of various host materials and rare-earth elements has been explored widely [31–34]. The smaller ionic size of the Li^+ ion allows it to occupy substitutional as well as interstitial sites, thereby tailoring the local crystal field and thus increasing the emission intensity of the material. Many reports propose that the incorporation of Li^+ ion results in a significant alteration in the crystallinity of the host phosphor [31,32]. These reports encourage the use of Li^+ ions for improving luminescence properties. The effect of Li^+ on the luminescence and structural property of the zinc vanadate is not investigated to date and is thus explored by us.

Material and methods

Phosphor synthesis

The precursors for the phosphor synthesis were $Zn(NO_3)_2{\cdot}6H_2O$ (99%, SRL chemicals), NH_4VO_3 (Sigma-Aldrich, 99%), and $LiNO_3$ (Sigma-Aldrich, 99.99%). The phosphors were synthesized by the sol–gel method using citric acid (Sigma-Aldrich, 99.5%). The $Zn_{(3-x)}Li_x(VO_4)_2$ (x = 0, 0.01, 0.02, 0.03) samples are assigned with code names L0, L1, L2, and L3, respectively. To begin with, a stoichiometric amount of ammonium metavanadate and metal nitrates were added to distilled water (100 ml) and stirred for 1 h. Several minutes after, the solution turns pale yellow and the temperature was increased to 80 °C. Later, the solution was supplemented with citric acid (molar ratio of metal ion/citric acid is 1:2), making it transparent and yellow. The color of the solution turns blue after stirring it for another 1 h and then the excess water was evaporated. The dried gel was kept at 250 °C for 12 h, followed by annealing at 700 °C for 4 h in a furnace. The obtained powder sample was further characterized. The synthesis process is presented schematically in Fig. 1.

Characterisation

The XRD data of the phosphors were obtained using Rigaku-MiniFlex 600 desktop x-ray diffraction system having with Cu K_α radiation source ($\lambda = 1.54$ Å). The phase purity and crystal structure was validated by the use of FULLPROF software [35]. The vibrational modes of the phosphors were determined from FTIR scans, obtained using a JASCO FT/IR 4600 spectrometer coupled with the Attenuated total reflection (ATR) setup, which includes a diamond disc as an internal reflection component. Prior to each sample examination, the spectrum of air was employed as a backdrop. Field emission scanning electron microscopy is utilized to inspect the morphology of the produced samples analysis, which is performed using Nova Nano SEM 450, USA. The average particle was calculated using ImageJ computer software. The UV–Vis absorption spectroscopy of the prepared powder samples was performed with the integrating sphere setup attached to the JASCO V770 spectrophotometer. The UV–Vis absorption spectra were recorded in absorbance mode after baseline correction using barium sulphate. The Photoluminescence emission (PL), photoluminescence excitation (PLE), and Temperature-dependent PL (TDPL) spectra were fetched using the Horiba Fluorolog-3 spectrophotometer. The PL and PLE spectrum of all the prepared phosphors were recorded for the slit width fixed at 1 nm. The PL lifetime measurement was done using the FLS920 spectrometer (Edinburgh Instruments) equipped with a 60 W xenon flash lamp. The absolute PL quantum yield measurement was done with the help of Horiba PTI QuantaMaster-400 fluorescence spectrometer equipped with an integrating sphere. Thermo Fischer Scientific ESCALAB Xi X-ray photoelectron spectrometer was used for XPS measurements.

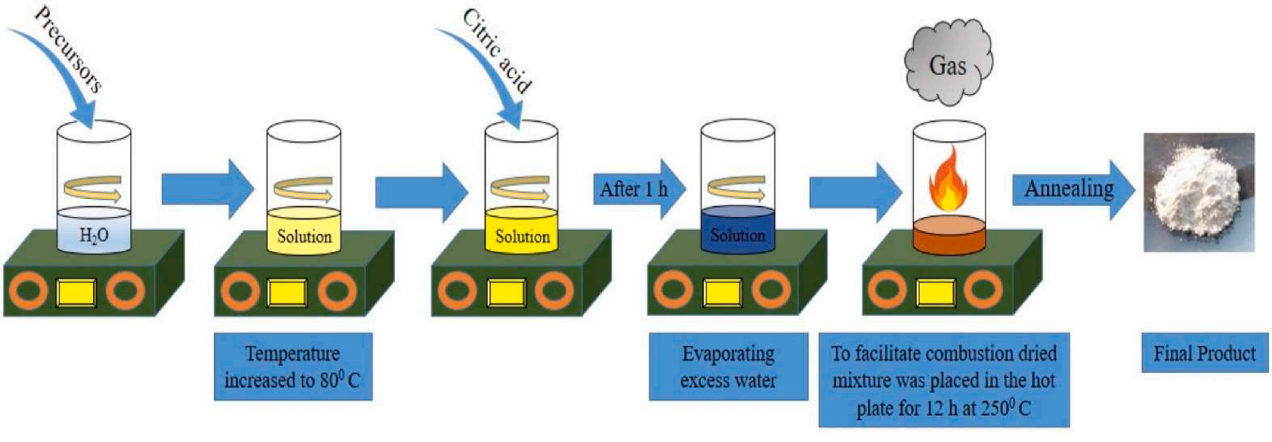

Fig. 1. Schematic of the synthesis process.

Results and discussion

Structural analysis

XRD study

The formation of solid solution and crystalline phase of the samples are authenticated by the XRD data analysis. The XRD study confirms the orthorhombic phase (JCPDS card no. 34–0378) of the prepared phosphors with symmetry described by the space-group of Cmca. The Rietveld refined XRD patterns of all produced phosphors are shown in Fig. 2 (a). Some of the prominent peaks for L0 are indexed in Fig. 2(a). It is observed that the most intense peak for the host sample (L0) is located at 34.92^0 which is indexed as (221). Further, by increasing the Li^+ doping, the intensity of peaks at 15.4^0 and 31.04^0 indexed as (020) and (040), respectively, is increased compared to the (221) peak. The height of the diffraction peak is influenced by the preferential crystal orientation and therefore the increased height of the (020) and (040) plane compared to the (221) plane indicates that the particles become more oriented towards (020) and (040) plane with increasing Li^+ concentration. Moreover, no extra impurity peak corresponding to Li^+ is observed. The crystal structure obtained after refinement and modeled using VESTA software is depicted in Fig. 2(b). The Zn^{2+} ions are present in the two octahedral sites, while V^{5+} ions occupy tetrahedral sites. The Zn^{2+} ions with 2/*m* symmetry have two different bond lengths, while Zn ions with *m* symmetry have three different bond lengths with oxygen [21]. Table 1 summarises the atomic coordinates of the component atoms, lattice parameters, unit cell volume, and bond lengths derived following Rietveld refinement. Fig. 2(c) presents the variation in the full-width half maximum (FWHM) for the (020) peak of all the phosphors. It is observed that the FWHM of the peak is decreased with Li^+ doping which indicates increased crystallinity of the phosphors [31].

The Williamson-Hall (W-H) equation is utilized for approximating the average crystallite size (*D*) and lattice strain (∈) of the phosphors. The Williamson-Hall equation is given by the following relation [21],

$$\beta_{hkl}cos\theta = 4\epsilon sin\theta + \frac{K\lambda}{D}$$

where the sum of microstrain broadening and crystallite size broadening is given by the resultant peak broadening (β_{hkl}), *K* resembles the crystallite shape factor, λ is the wavelength of the radiation, and θ denotes the Bragg angle. Fig. 3 presents the W-H plot for all the phosphors. The crystallite size (*D*) obtained from the slope of the linearly fitted line for L0, L1, L2, and L3 is 58 nm, 60 nm, 64 nm, and 69 nm, respectively. An augmentation in crystallite size value suggests that Li^+ ions favour the growth of crystallites and increase crystallinity [31–33]. The improvement in the crystallinity help in enhancing the emission intensity. The lattice strain is obtained from the intercept of the fitted straight line. The obtained value of lattice strain for L0, L1, L2, and L3 is 3.84×10^{-4}, 3.60×10^{-4}, 6.34×10^{-4}, and 9.86×10^{-4}, respectively.

FTIR spectroscopy analysis

The vibrational bands of phosphors are detected and analysed using FTIR spectrum. The FTIR spectra of unoped and Li^+ doped $Zn_3(VO_4)_2$ in the wavenumber range of 360 cm^{-1} to 3000 cm^{-1} are depicted in Fig. 4 and the band assignment for the respective wavenumber range is arranged in Table 2. The band in the region 410–426 cm^{-1} for L0 is ascribed to Zn-O stretching vibrations from ZnO_6 octahedra [30,36]. It is observed that there is a shift in Zn-O stretching vibrations towards the higher wavenumber side for doped samples, which is attributed to Li^+ doping in the host. The intense broadband around 516–724 cm^{-1} is ascribed to VO_4 tetrahedral vibrational modes [30]. The band observed at 782 cm^{-1} corresponds to Zn-O-V and V-O-V asymmetric vibrations [12,36]. The vibrational band around 808–852 cm^{-1} is accredited to V-O stretching vibration [37]. The vibrational bands attributed to VO_4 groups remain unaltered with Li^+ doping. The observed vibrational bands support the formation of the orthorhombic crystal structure of $Zn_3(VO_4)_2$ and are in accordance with previously stated values [21,36]. The band at 2363 cm^{-1} corresponds to CO asymmetric stretching vibration [21].

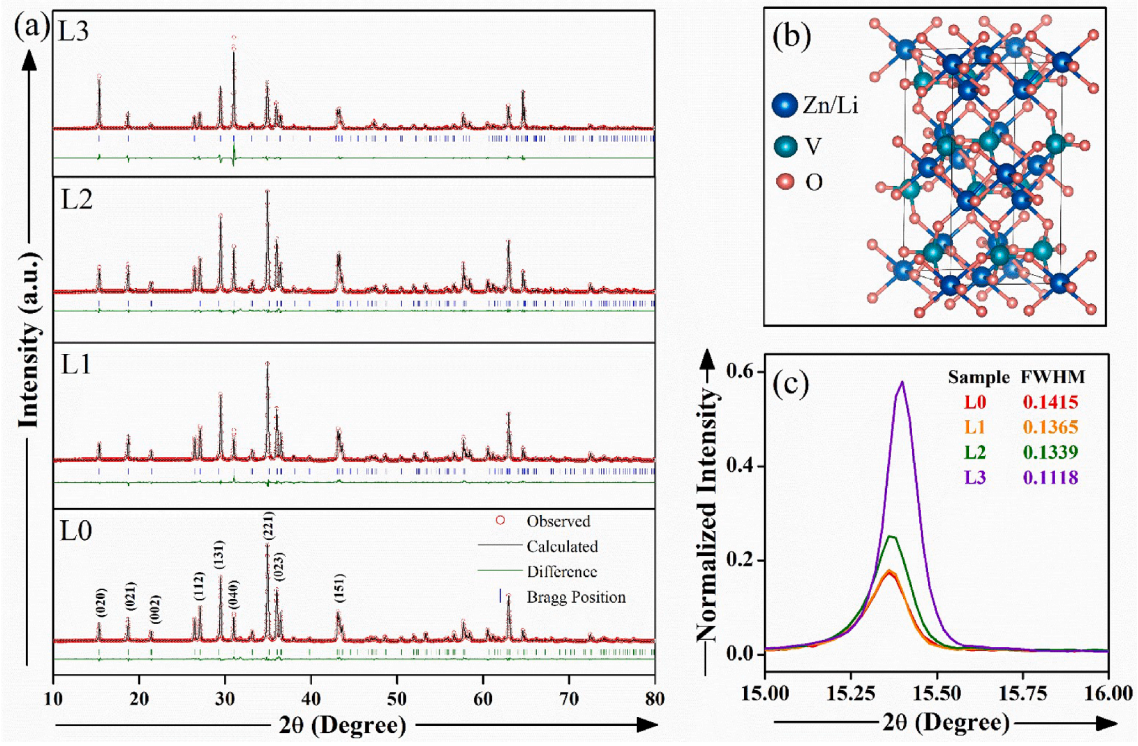

Fig. 2. (a). Rietveld refined XRD patterns of samples. **(b)** Crystal structure of the samples based on refinement data. **(c)** The alteration in the peak intensity and FWHM of (020) peak in 2θ for all prepared samples.

Table 1
Structural parameters for all the phosphors derived after Rietveld refinement of their individual XRD patterns.

Parameters	L0	L1	L2	L3
Atomic positions:				
Zn1/Li1				
(x,y,z)Zn2/Li2	(0, 0, 0)	(0, 0, 0)	(0, 0, 0)	(0, 0, 0)
(x,y,z)V	(0.25, 0.136,	(0.25, 0.136,	(0.25, 0.134,	(0.25, 0.127,
(x,y,z)O1	0.25)	0.25)	0.25)	0.25)
(x,y,z)O2	(0, 0.377,	(0, 0.377,	(0, 0.377,	(0, 0.382,
(x,y,z)O3	0.122)	0.121)	0.120)	0.119)
(x,y,z)	(0, 0.250,	(0, 0.251,	(0, 0.244,	(0, 0.238,
	0.230)	0.228)	0.235)	0.238)
	(0, 1.000,	(0, 0.996,	(0, 0.999,	(0, 0.991,
	0.246)	0.239)	0.240)	0.233)
	(0.222,	(0.216,	(0.215,	(0.215,
	0.379,	0.379,	0.381,	0.388,
	0.006)	0.007)	0.003)	0.005)
Angles (α, β, γ) in degree	(90, 90, 90)	(90, 90, 90)	(90, 90, 90)	(90, 90, 90)
Lattice parameters (Å)				
a	6.114	6.112	6.114	6.116
b	11.530	11.527	11.527	11.522
c	8.301	8.300	8.303	8.305
Unit cell volume ($Å^3$)	585.26	584.86	585.24	585.30
Bond lengths (Å)	2.050	1.992	1.999	1.942
(Zn1-O2)	(5)2.196	(0)2.222	(3)2.214	(0)2.163
(Zn1-O3)	(3)2.190	(0)2.221	(0)2.187	(0)2.194
(Zn2-O2)	(3)2.025	(0)2.031	(0)1.986	(0)1.992
(Zn2-O1)	(3)2.144	(0)2.157	(0)2.123	(0)2.137
(Zn2-O3)	(3)1.714	(0)1.699	(3)1.809	(0)1.929
(V-O1)	(4)1.787	(0)1.789	(0)1.809	(0)1.753
(V-O2)	(4)1.663	(0)1.627	(0)1.636	(0)1.626
(V-O3)	(3)	(0)	(0)	(0)
$R_{Factors}$				
R_p	8.32	8.95	6.92	10.6
R_{wp}	9.81	9.76	9.31	13.0
χ^2	3.13	3.05	5.14	12.3

FE-SEM analysis

The influence of Li^+ doping on the morphology of the zinc vanadate is investigated by FE-SEM study. The FE-SEM images of L0 and L2 samples are depicted in Fig. 5 (a) and (b), respectively. The particles in both samples are well distributed and exhibit little aggregation. The average particle size of L0 and L2 is 1.56 μm and 1.65 μm, respectively. Morphological analysis demonstrates that the average particle size is increased by Li^+ doping.

XPS analysis

XPS spectra is utilized to analyse the chemical composition and validation of oxidation states of the elements present on the surface of

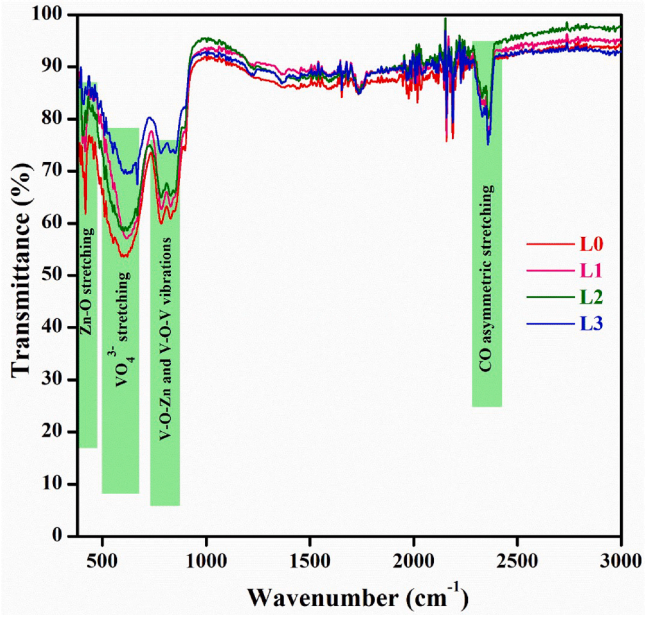

Fig. 4. FTIR spectra of all prepared phosphors.

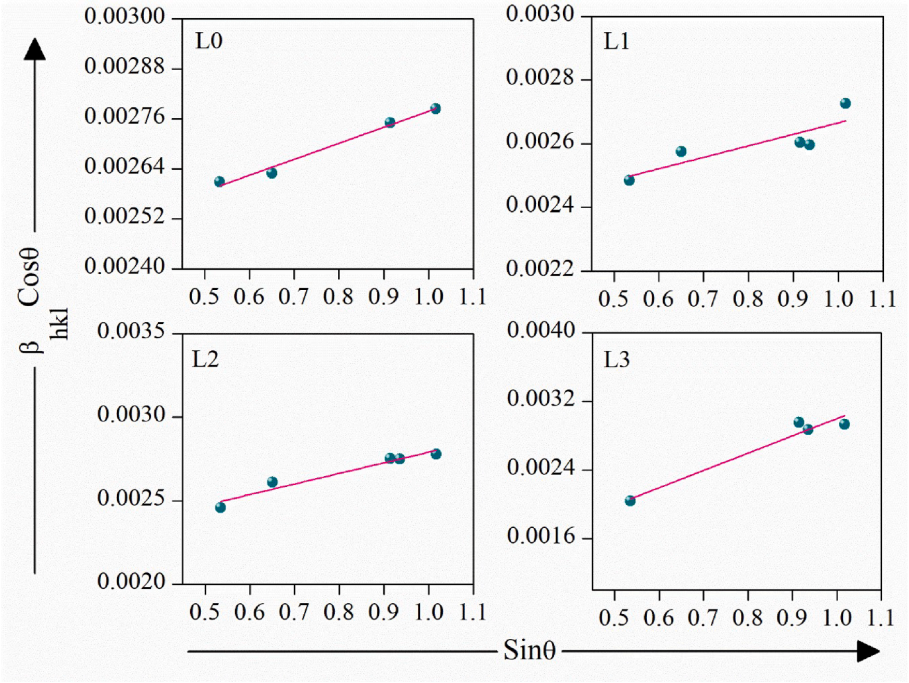

Fig. 3. Williamson-Hall plot for all the prepared phosphors.

Table 2
Vibrational modes assigned to different wavenumber bands observed in FTIR spectrum of samples.

Vibrational bands present in the phosphors (cm^{-1})				Vibrational mode assignments
L0	L1	L2	L3	
411–425	411–425	418–429	421–431	Zn-O stretching
516–724	516–724	516–724	516–724	VO_4 vibrational modes
782	782	782	782	Zn-O-V asymmetric and V-O-V vibrations
808–850	808–850	808–850	808–850	V-O stretching vibration
2364	2364	2364	2364	CO asymmetric stretching

the sample. All XPS data from all elements were charge adjusted for C1s. (~284.6 eV). The survey scan depicted the Fig. 6 (a) for the L2 sample confirms the presence of all prominent peaks corresponding to Zn, V, and O. All peaks in the survey scan are assigned per the national institute of standard technology (NIST) database. The survey scan also validates that there is no additional contaminant in the sample other than carbon. The carbon peak is present because of its absorption on the surface of the sample during air exposure. Fig. 6 (b), (c), (d), and (e) depicts the XPS spectra of V (2p), Li (1s), Zn (2p), and O (1s) for L2 sample. The high-resolution core-level spectrum in Fig. 6 (b), shows peaks corresponding to V (2p) having BE of ~516.97 eV ($2p_{3/2}$) and ~524.47 eV ($2p_{1/2}$) with doublet separation (Δ) of about ~7.4 eV. This confirms that the vanadium present in the sample is in the V^{5+} oxidation state [12,30,36,38]. The XPS spectrum of Li (1s) confirms the presence of Li 1s peak at 54.37 eV [39,40]. The symmetric peak corresponding to Zn (2p) has a core BE of ~1021.37 eV ($2p_{3/2}$) and ~1044.47 eV ($2p_{1/2}$), corroborating that Zn is in Zn^{2+} oxidation state [12,30,41]. The peak at ~529.97 eV corresponds to O (1s) [38,41]. The O1s peak is deconvoluted into two peaks at ~529.95 eV and 531.46 eV, which is accredited to lattice oxygen and surface adsorbed oxygen (i.e. O^-, O_2^-, O_2^{2-}), respectively [38]. The details of XPS spectra confirm that the pure phase of $Zn_3(VO_4)_2$ is formed.

Optical study

UV–Vis absorption analysis

Fig. 7 presents the absorption spectrum of the samples. The absorption band of the prepared phosphors occurs in the near UV region from 300 nm to 450 nm and is centered at 375 nm. The strong absorption in the near UV region ascertains that the prepared phosphors have a strong affinity to absorb near UV photons. The doping of Li^+ has not shifted the peak position of the absorption band. The broad absorption peak is attributed to the ligand to the metal charge transfer band (CTB). The CTB is formed as a result of the charge transfer from O^{2-} to V^{5+} in $[VO_4]$ tetrahedral. The absorption CTB is broadened after Li^+ doping.

The bandgap energy (E_g) for all the phosphors can be evaluated using the following Tauc relation [42]:

$$\alpha h\vartheta = A(h\vartheta - E_g)^n$$

where α denotes the absorption coefficient and $h\vartheta$ is the photon energy. The $Zn_3(VO_4)_2$ phosphor has a direct allowed electronic transition and therefore n is taken to be ½ [42]. The bandgap of all the phosphors is determined by the x-intercept of the extrapolated linear part of $(\alpha h\vartheta)^2$ versus $(h\vartheta)$ plot and is presented in the inset of Fig. 7. The bandgap energy of L0 is estimated to be 2.96 eV and a slight increment in bandgap is observed with Li^+ doping in the host lattice.

The doping-induced disorder in the $Zn_3(VO_4)_2$ can be validated by examining the variation in Urbach energy (E_u). The E_u is evaluated by the following relation [43],

$$\alpha = \alpha_0 e^{\left(\frac{h\vartheta}{E_u}\right)}$$

where α_0 is a constant. The E_u is evaluated from the reciprocal of the slope of the linear part of $\ln(\alpha)$ vs $h\vartheta$ plot. The $\ln(\alpha)$ vs. $h\vartheta$ plot for L0 is depicted in Fig. 7 (b) and the inset shows the variation in Urbach energy. The E_u for L0 is 0.42 eV and decreases with Li^+ doping. The decrease in E_u with Li^+ doping is a good indication of the increased crystallinity of the samples [21,44].

Photoluminescence analysis

The PLE spectrum for $Zn_3(VO_4)_2$ and Li^+ doped $Zn_3(VO_4)_2$ samples, examined at 542 nm emission wavelength is presented in Fig. 8 (a). The PLE spectrum for all the phosphors exhibits similar absorption broadband ranging from 280 nm to 400 nm. The absorption band in vanadate compounds is attributed to $(VO_4)^{3-}$ groups [17,45]. The molecular orbitals of a V^{5+} ion with T_d symmetry comprise a ground state $^1A_1$, and four excited states, whose energies lie in the order of $^1T_2 > {}^1T_1 > {}^3T_2 \sim {}^3T_1$, as depicted in Fig. 9 (e) [18,45]. The Deconvoluted Gaussian fitting of the PLE spectrum for L0 and L2 are shown in Fig. 9 (a) and (c), respectively. The Deconvoluted PLE spectrum for L0 exhibit three absorption bands centered at 3.32 eV (Ex1), 3.55 eV (Ex2), and 4.02 eV (Ex3). Not much variation in the peak position of Ex1, Ex2, and Ex3

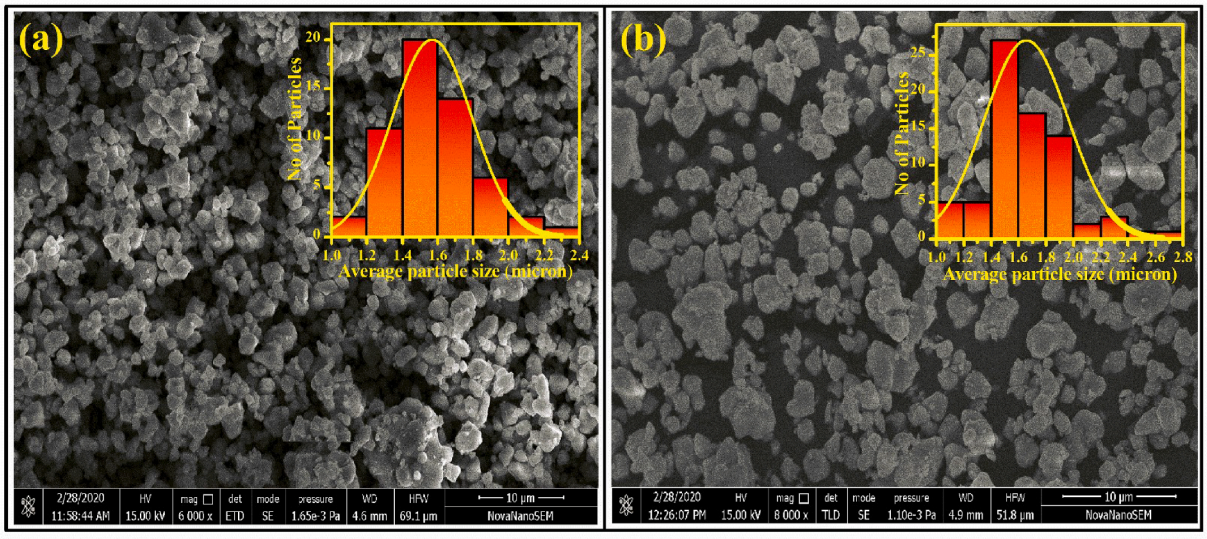

Fig. 5. FE-SEM micrographs of (a) L0 and (b) L2.

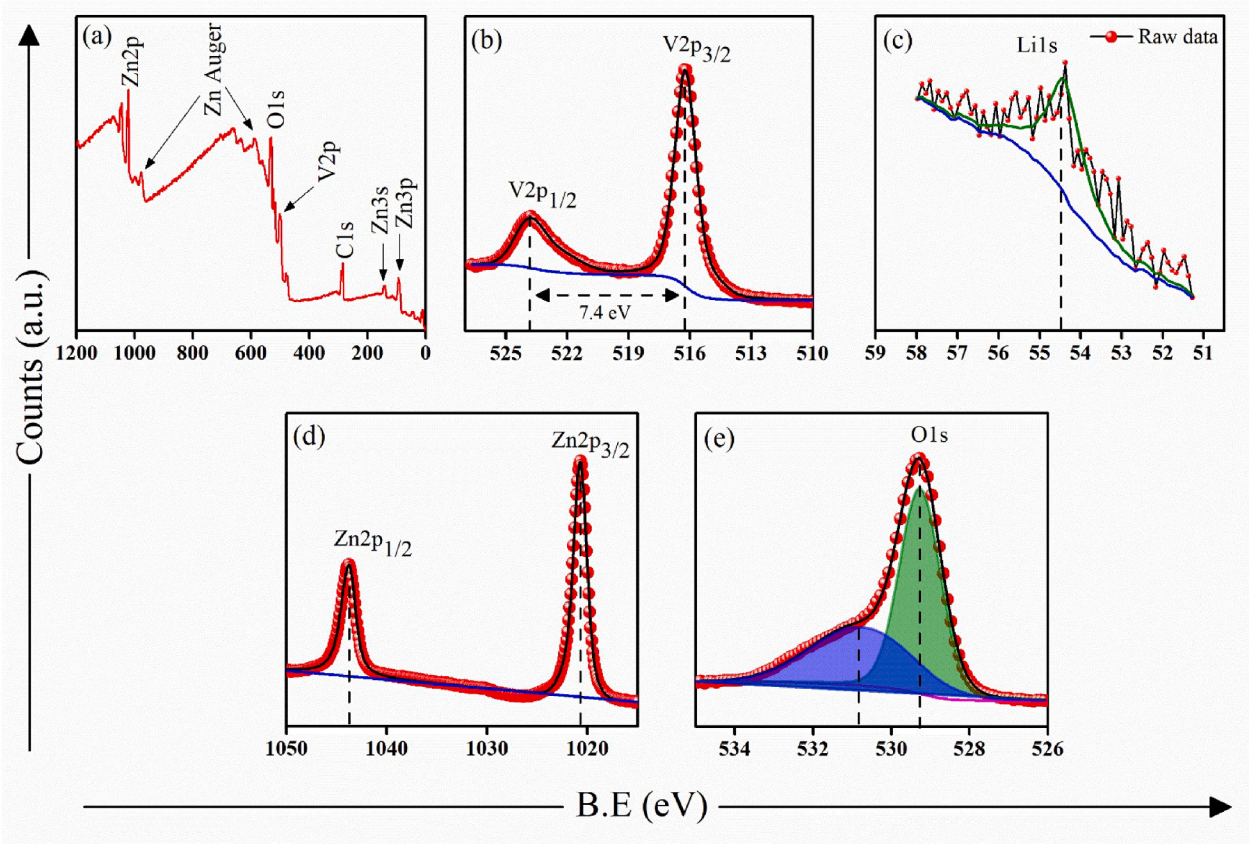

Fig. 6. (a) XPS survey scan for L2. XPS spectra of (b) V2p, (c) Li 1s, (d) Zn 2p, (e) O1s for L2.

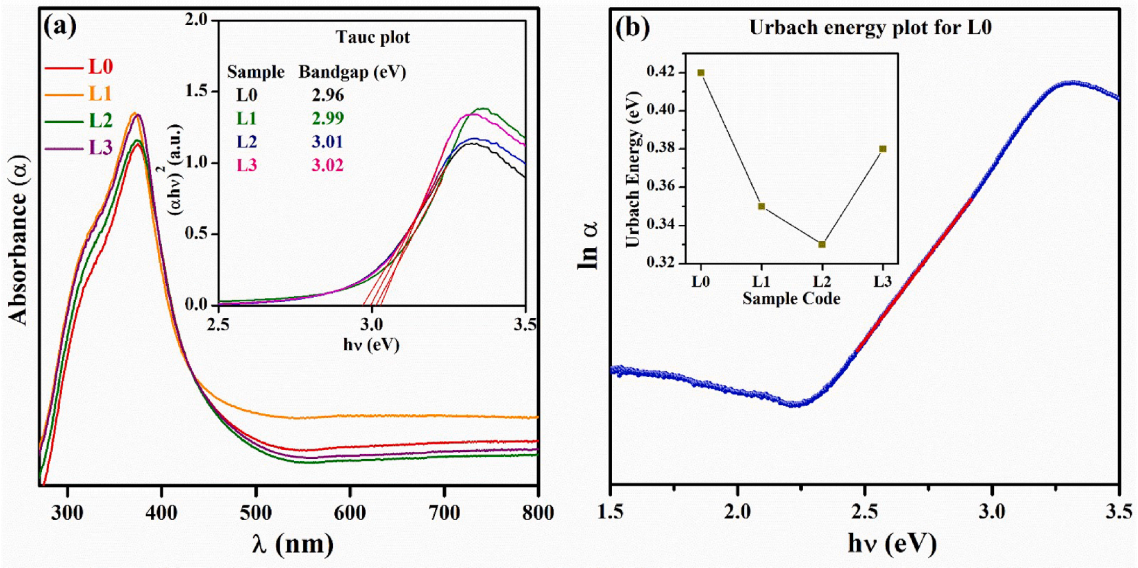

Fig. 7. (a) Absorbance spectrum of the samples. Inset shows Tauc plot and bandgap of all the phosphors. (b) Urbach energy plot for L0. The fluctuation of Urbach energy with Li^+ doped phosphors is depicted in the inset of (b).

peaks for L2 is observed but they have slightly increased FWHM as compared to L0 peaks. The Ex3 band is ascribed to $^1A_1 \rightarrow {}^1T_2$ electronic transition and the Ex2 band along with the shoulder Ex1 band corresponds to $^1A_1 \rightarrow {}^1T_1$ electronic transition [17,18,45,46]. It is observed that there is a rise in the PLE spectrum of Li^+ doped $Zn_3(VO_4)_2$ as compared to undoped $Zn_3(VO_4)_2$. The inset in Fig. 8 (a) depicts the variation of PLE spectrum intensity. The near UV excitation is essential for white light LED device application as it overlaps with the emission band of commercial near UV LED chips. Thus, together with near UV LED chips, the Li^+ doped $Zn_3(VO_4)_2$ phosphors can be utilized in wLED applications.

Fig. 8 (b) depicts the PL spectrum for $Zn_3(VO_4)_2$ and Li^+ doped $Zn_3(VO_4)_2$ samples examined at 360 nm emission wavelength. The PL spectrum for all the phosphors exhibits similar absorption broadband

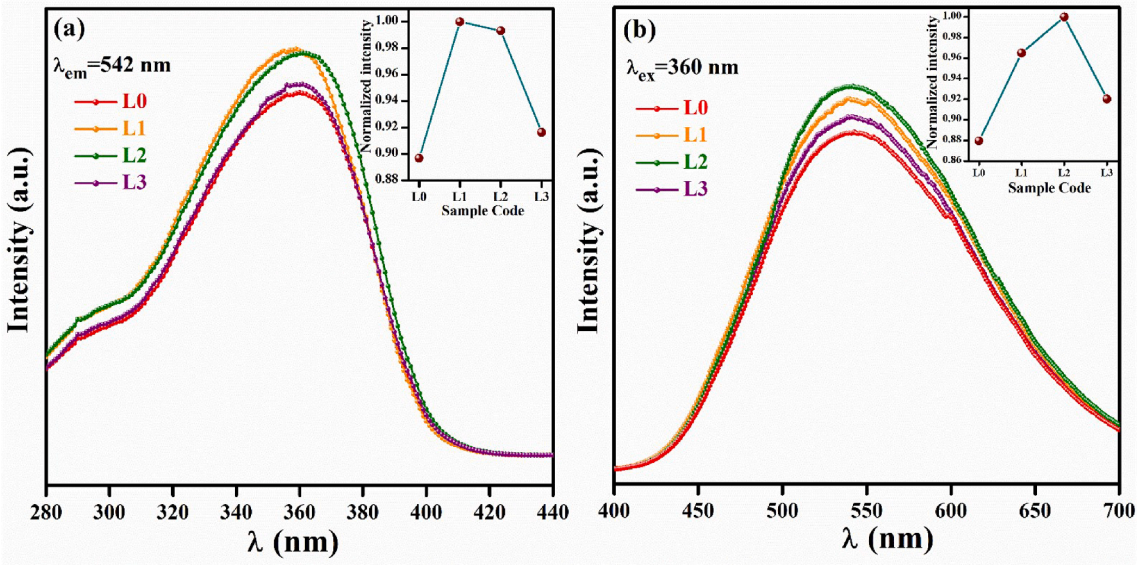

Fig. 8. (a) PLE spectra of the phosphors examined at 542 nm emission wavelength. Inset shows the variation of PLE spectrum intensity. (b) PL spectra of the prepared phosphors monitored at 360 nm excitation wavelength. Inset shows the variation of PLE spectrum intensity.

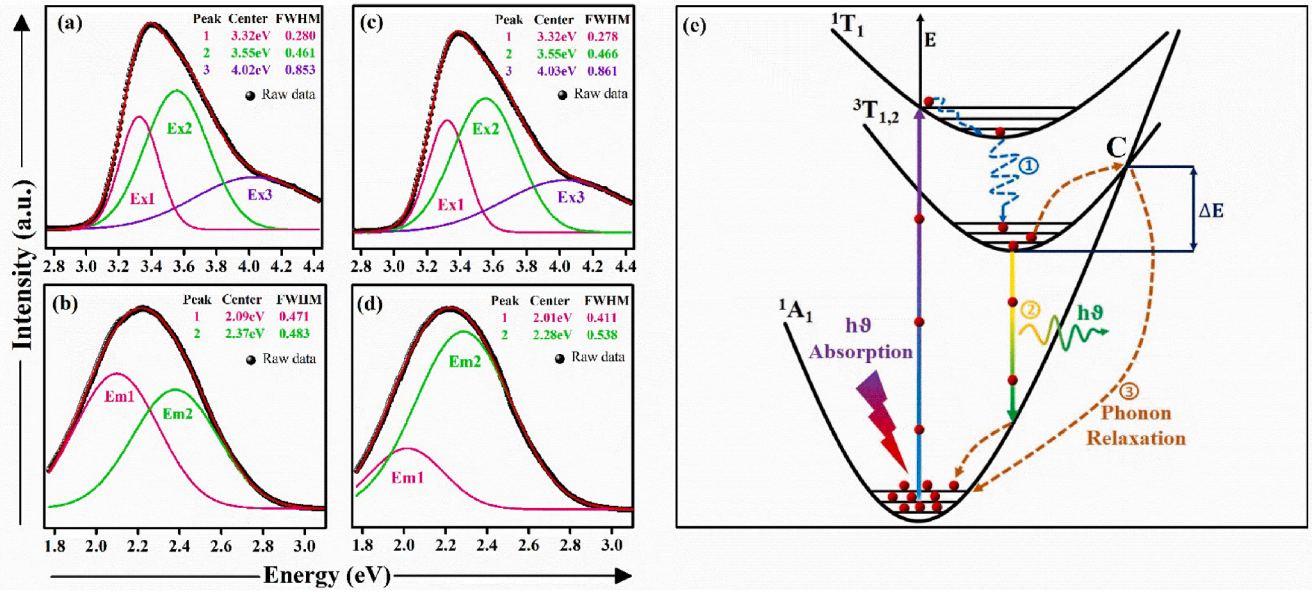

Fig. 9. Deconvoluted excitation peak (a) and emission peak (b) for L0. Deconvoluted excitation peak (c) and emission peak (d) for L2. (e) Configurational coordinate diagram for understanding absorption, florescence, and thermal quenching phenomenon.

ranging from 400 nm to 700 nm and centered at 542 nm, which is attributed to the charge transfer from the O 2p orbital to the vacant 3d orbital of V^{5+} ion. The emission broadband is attributed to electronic transitions of $(VO_4)^{3-}$ groups, depicted in Fig. 9 (e). The deconvoluted Gaussian fitting of the PL spectrum for L0 and L2 are dpicted in Fig. 9 (b) and (d), respectively. The deconvoluted PL spectrum for L0 exhibits two emission bands centered at 2.09 eV (Em1) and 2.37 eV (Em2), which corresponds to $^3T_1 \rightarrow {}^1A_1$ and $^3T_2 \rightarrow {}^1A_1$ electronic transitions, respectively [47]. In comparison to L0, the peak position of Em1 and Em2 bands for L2 are red-shifted with the Em1 band overlapping with the Em2 band. The Stokes shift, Δ S, is the energy gap between the excitation edge and the emission band edge. The evaluated Δ S for L0 is 9436.68 cm^{-1} and for L2 it is 9517.33 cm^{-1}. The value of Δ S for L0 and L2 is greater than the commercial phosphors and other reported vanadate phosphors [46,48]. The phosphors with large Δ S values provide white-light emission with uniform hue, high CRI and it reduces self-quenching that results from self-absorption in phosphors [46]. Thus, L0 and L2 phosphors have large Δ S values, which is beneficial for white-light indoor illumination.

Role of Li^+ in enhancing the PL intensity

As shown in Fig. 8 (b), the PL emission of Li^+ doped $Zn_3(VO_4)_2$ is enhanced as compared to undoped $Zn_3(VO_4)_2$. In perfect VO_4 tetrahedral T_d symmetry, the luminescence process ($^3T_1$,$^3T_2 \rightarrow {}^1A_1$) is forbidden by the spin selection rule. However, in crystal lattices such as $Zn_3(VO_4)_2$, the T_d symmetry is distorted and $^3T_1 \rightarrow {}^1A_1$ and $^3T_2 \rightarrow {}^1A_1$ electronic transitions become partially allowed [27]. The doping of Li^+ ions in $Zn_3(VO_4)_2$ lattice creates variation in the crystal lattice field surrounding the $(VO_4)^{3-}$ groups owing to the difference in ionic radius of Zn^{2+} and Li^+ ions. This may consequently influence the spin–orbit coupling and distort VO_4 tetrahedron even more from the ideal thereby increasing the luminescence in Li^+ doped $Zn_3(VO_4)_2$ [27]. The increase in emission

intensity of L2 compared to L0 is also attributed to the increase in crystallinity, improved crystallite size, and increase in particle size after Li^+ doping. The XRD study reveals that the crystallinity of the host sample is improved with Li^+ doping. The improved crystallinity contributes toward the PL enhancement. The defect centers present on the surface of the particles act as quenching centers for the excited ions, as these defects absorb some of the energy and then prompt ions to relax non-radiatively to their ground state. Thus, with the increase in defect centers, the non-radiative relaxation of ions also increases. It is observed that the increased crystallinity helps in increasing the particle size of the phosphors and therefore decreases the surface-to-volume ratio [43]. As more defect centers are present on the surface of the particles, the decrease in the total surface area of the particle decreases the interaction between the defect centers and the ions. Therefore, the overall number of radiative ions in the crystallites increases thereby increasing the emission intensity [31,32,43,49]. The increase in PLE intensity also contributes to the increase in PL intensity after Li^+ doping. The emission intensity decreases for the L3 sample as a further increase in Li^+ content prompts Li^+ ions to occupy interstitial sites, which creates defects in the crystal and therefore leads to luminescence quenching.

Decay curve analysis

The PL decay curves of L0 and L2 phosphors recorded upon 360 nm excitation and 542 nm emission are depicted in Fig. 10 (a) and (b), respectively. The decay curves were examined by fitting them with the single exponential function as determined by the following equation [50],

$$I(t) = I_0 exp\left(-\frac{t}{\tau}\right)$$

where, τ is the lifetime of Em1 and Em2 emission bands accredited to the electronic transitions of the $[VO_4]^{3-}$ group. The value of τ for L0 and L2 phosphors is 146 μs and 158 μs, respectively. Thus, it is observed that the lifetime is increased after Li^+ doping. The increased lifetime is attributed to the improved crystallinity in the L2 phosphor. The defect centers operate as luminescence quenchers because the emitting ions lose part of their energy to these defect centers and revert non-radiatively to the ground state. The improvement in crystallinity in the L2 phosphor is an indication of the reduction of defect centers. Thus, by improvement in crystallinity, the probability of non-radiative relaxation of the emitting ions is reduced and the average lifetime of emitting ions is increased. [14,32,50-52]. It has also been discovered that the average particle size has grown after 2% Li^+ co-doping. The increase in particle size reduces the surface-to-volume ratio and the overall grain boundaries. As the defect centers are comparatively more on the surface, therefore with the decrease in surface area and the overall grain boundaries, the number of emitting ions interacting with them also decreases, and the average lifetime of emitting ions increases [50,52]. The analysis of decay curves validates improvement in crystallinity which consecutively supports the increase in the emission intensity of $Zn_3(VO_4)_2$ phosphor in the presence of Li^+ ions.

CIE and CCT analysis

The Commission Intentional de I'eclairage (CIE) chromaticity coordinates for L0 and L2 are plotted in the CIE diagram depicted in Fig. 11. The evaluated CIE coordinates (x, y) for L0 and L2 are (0.366, 0.481) and (0.368, 0.485), respectively. As presented in the CIE diagram, the overall emission of the prepared phosphors is greenish-yellow. The value of color correlated temperature (CCT) has been estimated using the following McCAMY's expression [31,53],

$$CCT = 5520.33 - 6823n + 3525n^2 - 449n^3$$

where $n = \frac{(x-x_e)}{(y-y_e)}$ is the inverse slope line, (x, y) is the CIE coordinates, and

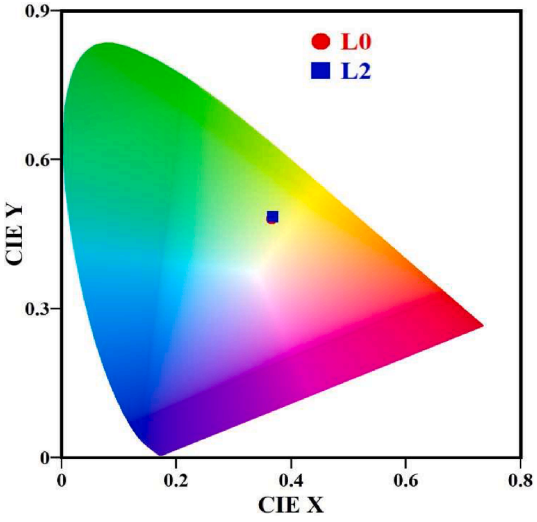

Fig. 11. Chromaticity diagram depicting CIE coordinates of L0 and L2 phosphors.

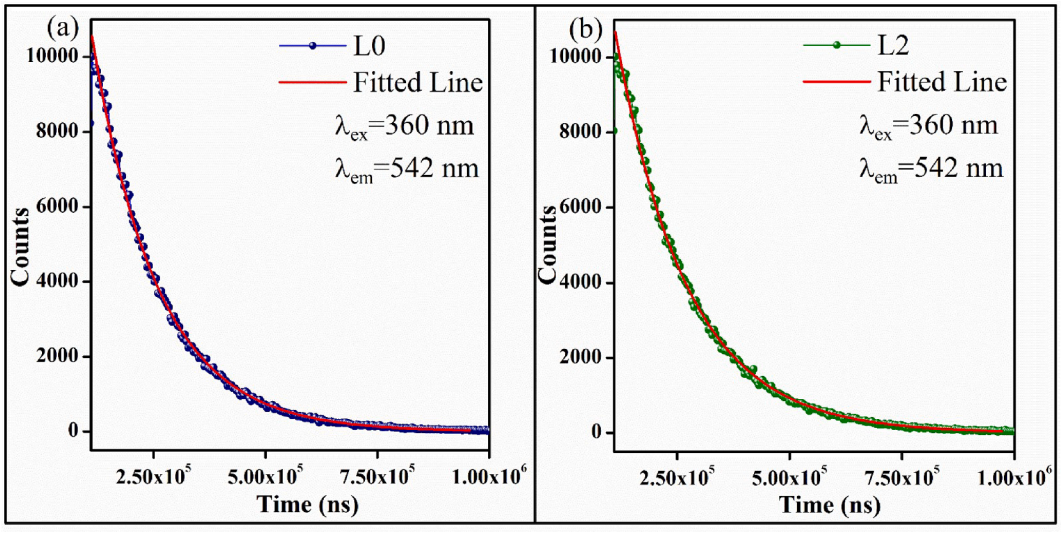

Fig. 10. PL decay curves of (a) L0 and (b) L2 samples, recorded upon 360 nm excitation and 542 nm emission.

(x_e, y_e) are the chromaticity epicenter (0.338, 0.186). The calculated CCT from the above equation for L0 and L2 is 4906 K and 4871 K, respectively.

Temperature-dependent PL and absolute quantum yield analysis

The investigation of the thermal stability of the phosphor is vital for its technological utilization. In this regard, we have analyzed the thermal quenching phenomenon in the L2 sample. Fig. 12 (a) depicts the temperature-dependent PL emission spectra of L2 phosphor in the temperature range of 30 °C – 180 °C. It is evident that with rising temperature there is a gradual decrease in the PL intensity. Any shift in the PL spectra is not observed with rising temperatures which is desirable for lighting applications. The decrease in PL intensity with rising temperatures is ascribed to the non-radiative phonon relaxation of the electrons from the higher energy levels [18]. Fig. 12 (b) represents the variation of integrated intensity with rising temperatures. The emission intensity at 150 °C is about 56% of the intensity at 30 °C. Therefore, there is a 44% loss of emission intensity at 150 °C, which is better than some of the reported vanadate phosphors [11,18,54–56].

The influence of the thermal quenching on the emission spectra can be further examined by evaluating the ΔE from the following Arrhenius equation [54],

$$I_T = \frac{I_0}{1 + Ae^{(-\Delta E/kT)}}$$

where I_0 is the emission intensity at 303 K, I_T is the emission intensity at temperature T (Kelvin), k is the Boltzmann constant (8.629 x 10^{-5} eV/K), and A is the constant frequency factor. The $\ln\left(\frac{I_0}{I_T}-1\right)$ vs 1/kT plot, as shown in Fig. 12 (c), is linearly fitted and the slope of the fitted line gives the value of ΔE. The obtained value of ΔE is 0.29 eV. The calculated activation energy of Li^+ doped $Zn_3(VO_4)_2$ phosphor is greater than earlier reported $Zn_3(VO_4)_2$ [27]. The relatively high value of activation energy demonstrates that L2 phosphor has good thermal stability. The good thermal stability of the phosphor is required to avoid overall emission color shifting. The influence of rising temperature on the emission color is explored by examining the CIE chromaticity coordinates of the L2 phosphor at different temperatures. As depicted in Fig. 12 (d), there is no remarkable change in the color coordinates under high temperatures. This conclusion is important as stable emission color under working temperatures is desirable for the application of the near UV wLED application. The absolute PL quantum yield of the L2 phosphor was also evaluated with the help of an integrating sphere monitored at 560 nm excitation wavelength and it was obtained as 4.60%.

Configurational coordinate diagram

The process of absorption, fluorescence, and thermal quenching in the $Zn_3(VO_4)_2$ can be elucidated by the configurational coordinate diagram depicted in Fig. 9 (e). The molecular orbitals of $[VO_4]^{3-}$ in $Zn_3(VO_4)_2$ are expressed as $^1A_1$ ground state and $^3T_1$, $^3T_2$, $^1T_1$, $^1T_2$ excited states [45]. During the process of photoabsorption (360 nm), electrons jump to excited states by following $^1A_1 \rightarrow {}^1T_1$, $^1T_2$ allowed transitions in T_d symmetry. The electrons are relaxed to the equilibrium position in the ^3T state by the process of vibrational relaxation and internal conversion (path (1) in Fig. 9 (e)). Due to the spin selection criterion, the $^3T_1$, $^3T_2 \rightarrow {}^1A_1$ transitions are ideally forbidden in T_d symmetry. However, the T_d symmetry is distorted from the idealized tetrahedron and by spin–orbit interaction, the $^3T_1$, $^3T_2 \rightarrow {}^1A_1$ transitions become partially allowed. As a result, the electrons revert to the $^1A_1$ ground state by following path (2) in Fig. 9 (e) and giving Em1 and Em2 emission bands (see Fig. 9 (b) and (d)). As the temperature is raised, the lattice vibrations are strengthened which increases the thermally active phonons. After coupling with the thermally active phonons, the energy of the excited electrons at the bottom of the $^3T_{1,2}$ band can approach crossover point C. These electrons revert to the ground state non-radiatively by following the path (3) [19]. With the rising

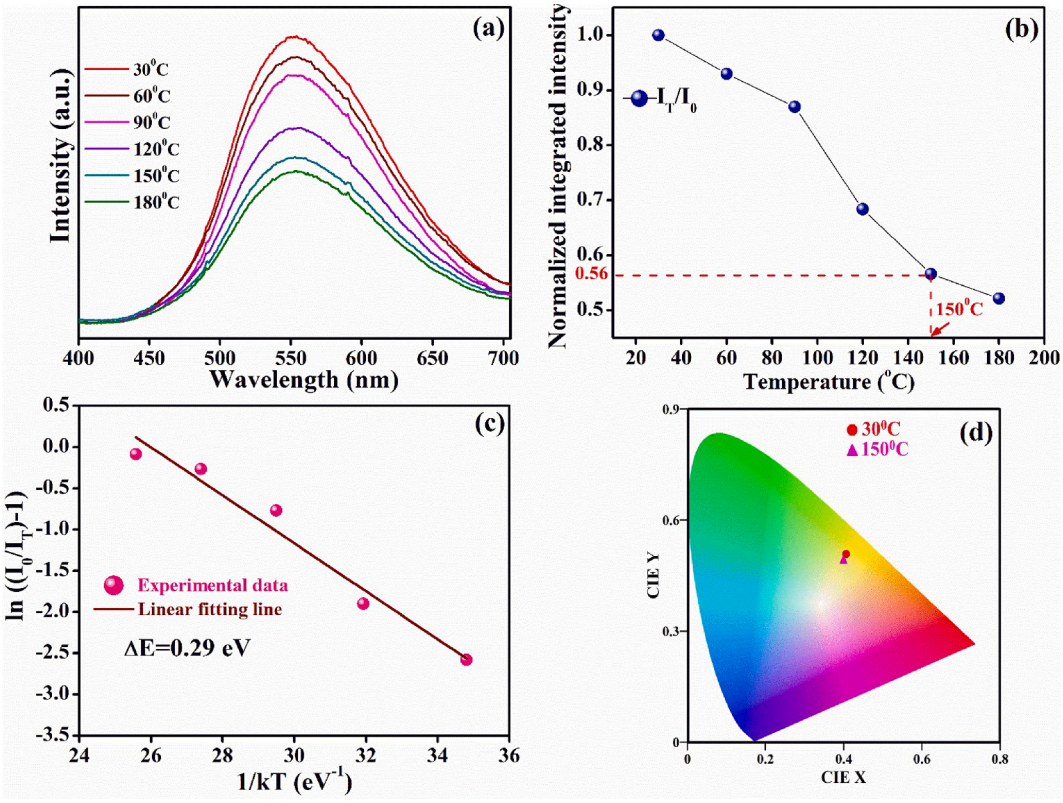

Fig. 12. (a) TDPL spectra of L2 phosphor, (b) Normalized integrated intensity plot as a function of temperature, (c) $\ln\left(\frac{I_0}{I_T}-1\right)$ vs 1/kT plot, and (d) CIE chromaticity diagram depicting variation in CIE coordinates with temperature for L2 phosphor.

temperature, the electron–phonon interaction increases and more electrons cross ΔE barrier, thereby reaching point C and relaxing non-radiatively to the $^1A_1$ ground state.

Conclusion

In summary, we have studied the luminescence and structural properties of the undoped and Li^+ doped $Zn_3(VO_4)_2$ successfully prepared by the citrate sol–gel technique. The XRD study ascertains the orthorhombic crystal structure of prepared phosphors, which is well supported by FTIR spectroscopy analysis. The XRD analysis substantiates improvement in crystallinity for Li^+ doped samples. The W-H plot analysis ascertains an increase in crystallite size for Li^+ doped phosphors. The FE-SEM analysis confirms the augmentation in particle size after Li^+ doping. The XPS examination validates the oxidation states of the elements present in the Li^+ doped phosphor. The excitation of the prepared phosphors lies in the near-UV region and the overall emission is greenish-yellow. Thus, these phosphors can be used with the commercially available near-UV emitting LED chips for the wLEDs application. The Li^+ doping further enhances the PLE and PL intensity of the $Zn_3(VO_4)_2$ phosphors. The increase in emission is accredited to the improved crystallinity, increased particle size, and increased light absorption by Li^+ doping. The decay curve analysis validates improvement in crystallinity which consecutively supports the enhancement in the PL intensity of $Zn_3(VO_4)_2$ as a result of Li^+ doping. The calculated activation energy of the Li^+ doped $Zn_3(VO_4)_2$ is 0.29 eV, validating good thermal stability of the phosphor. Moreover, there is a 44% loss of emission intensity at 150 °C. We conclude that with near UV excitation, greenish-yellow emission, large Δ S value, good thermal stability, and cost-efficient synthesis process, the L2 phosphor is anticipated to be an excellent material for near UV-based white LEDs and other optoelectronic devices.

CRediT authorship contribution statement

Vaibhav Chauhan: Conceptualization, Data curation, Formal analysis, Investigation, Methodology, Writing – original draft. **Pratik Deshmukh:** Resources. **S. Satapathy:** Resources. **Praveen C. Pandey:** Supervision, Writing – review & editing, Resources.

Declaration of Competing Interest

The authors declare that they have no known competing financial interests or personal relationships that could have appeared to influence the work reported in this paper.

Acknowledgments

Vaibhav Chauhan is grateful to the CSIR, India, for financial assistance in the form of a senior research scholarship. The authors are grateful to DST-FIST for providing a UV-Vis spectrophotometer and FTIR spectrometer. The authors like to thank Dr. Manoj Kumar, Associate Professor, Department of Chemical Engineering and Technology, IIT (BHU), Varanasi-221005, India for absolute quantum yield measurement.

References

[1] Kuo YK, Chang JY, Tsai MC, Yen SH. Advantages of blue InGaN multiple-quantum well light-emitting diodes with InGaN barriers. Appl Phys Lett 2009;95:011116. https://doi.org/10.1063/1.3176406.
[2] Nishiura S, Tanabe S, Fujioka K, Fujimoto Y. Properties of transparent Ce:YAG ceramic phosphors for white LED. Opt Mater (Amst) 2011;33:688–91. https://doi.org/10.1016/j.optmat.2010.06.005.
[3] Peter S, Patel A, Kitai A. Photoluminescence enhancement of Ce:YAG nanophosphors via doped/intrinsic core/shell structures. J Lumin 2019;211:82–7. https://doi.org/10.1016/j.jlumin.2019.03.024.
[4] Pust P, Weiler V, Hecht C, Tücks A, Wochnik AS, Henß AK, et al. Narrow-band red-emitting Sr[LiAl3N4]:Eu2+ as a next-generation LED-phosphor material. Nat Mater 2014;13:891–6. https://doi.org/10.1038/nmat4012.
[5] Chen D, Xiang W, Liang X, Zhong J, Yu H, Ding M, et al. Advances in transparent glass–ceramic phosphors for white light-emitting diodes—a review. J Eur Ceram Soc 2015;35:859–69. https://doi.org/10.1016/J.JEURCERAMSOC.2014.10.002.
[6] Zhou Y, Chen D, Tian W, Ji Z. Impact of Eu3+ dopants on optical spectroscopy of Ce3+: Y3Al5O12-embedded transparent glass-ceramics. J Am Ceram Soc 2015;98:2445–50. https://doi.org/10.1111/JACE.13668.
[7] George NC, Pell AJ, Dantelle G, Page K, Llobet A, Balasubramanian M, et al. Local environments of dilute activator ions in the solid-state lighting phosphor Y3-xCexAl5O12. Chem Mater 2013;25:3979–95. https://doi.org/10.1021/CM401598N/SUPPL_FILE/CM401598N_SI_001.PDF.
[8] Dixit P, Chauhan V, Rai SB, Pandey PC. Realization of neutral white light emission in CaMoO4_4Dy3+ phosphor via Sm3+co-doping. J Alloys Compd 2022;897:162820. https://doi.org/10.1016/j.jallcom.2021.162820.
[9] Xie F, Zhang TA, Dreisinger D, Doyle F. A critical review on solvent extraction of rare earths from aqueous solutions. Miner Eng 2014;56:10–28. https://doi.org/10.1016/J.MINENG.2013.10.021.
[10] Pitale SS, Gohain M, Nagpure IM, Ntwaeaborwa OM, Bezuidenhoudt BCB, Swart HC. A comparative study on structural, morphological and luminescence characteristics of Zn3(VO4)2 phosphor prepared via hydrothermal and citrate-gel combustion routes. Phys B Condens Matter 2012;407:1485–8. https://doi.org/10.1016/j.physb.2011.09.067.
[11] Huang X, Wang S, Rtimi S, Devakumar B. KCa2Mg2V3O12: A novel efficient rare-earth-free self-activated yellow-emitting phosphor. J Photochem Photobiol A Chem 2020;401:112765. https://doi.org/10.1016/j.jphotochem.2020.112765.
[12] Sajid MM, Shad NA, Khan SB, Zhang Z, Amin N. Facile synthesis of Zinc vanadate Zn3(VO4)2 for highly efficient visible light assisted photocatalytic activity. J Alloys Compd 2019;775:281–9. https://doi.org/10.1016/j.jallcom.2018.10.134.
[13] Lin L, Jiang X, Wu C, Lin Z, Huang Z, Humphrey MG, et al. First chiral fluorinated lead vanadate selenite Pb2(V2O4F(VO2)(SeO3)3 with five asymmetric motifs and large optical properties. Dalt Trans 2021. https://doi.org/10.1039/d1dt00536g.
[14] Rai E, Yadav RS, Kumar D, Singh AK, Fulari VJ, Rai SB. Influence of Bi3+ ion on structural, optical, dielectric and magnetic properties of Eu3+ doped LaVO4 phosphor. Spectrochim Acta – Part A Mol Biomol Spectrosc 2020;243. https://doi.org/10.1016/j.saa.2020.118787.
[15] Miyazaki H, Mimaru Y. Flexible white-light-emitting thin-film CsVO3 devices obtained using cesium vanadate aqueous solution. Opt Mater (Amst) 2021;114:111004. https://doi.org/10.1016/j.optmat.2021.111004.
[16] Levine AK, Palilla FC. A new, highly efficient red-emitting cathodoluminescent phosphor (YVO 4:Eu) for color television. Appl Phys Lett 1964;5:118–20. https://doi.org/10.1063/1.1723611.
[17] E. Pavitra, G. Seeta Rama Raju, L. Krishna Bharat, J.Y. Park, C.H. Kwak, J.W. Chung, Y.K. Han, Y.S. Huh, Evolution of highly efficient rare-earth free Cs(1-: X) RbxVO3 phosphors as a single emitting component for NUV-based white LEDs, J Mater Chem C. 6 (2018) 12746–12757. https://doi.org/10.1039/c8tc05110k.
[18] Bharat LK, Jeon SK, Krishna KG, Yu JS. Rare-earth free self-luminescent Ca2 KZn2 (VO4)3 phosphors for intense white light-emitting diodes. Sci Rep 2017;7:1–9. https://doi.org/10.1038/srep42348.
[19] Zhou J, Huang F, Xu J, Chen H, Wang Y. Luminescence study of a self-activated and rare earth activated Sr3La(VO4)3 phosphor potentially applicable in W-LEDs. J Mater Chem C 2015;3:3023–8. https://doi.org/10.1039/c4tc02783c.
[20] Kim H, Kim J, Lim S, Park K. Photoluminescence of vanadate garnet Ca2NaMg2-xV3O12:xEu3+ phosphors synthesized by solution combustion method. J Nanosci Nanotechnol 2016;16:1827–30. https://doi.org/10.1166/jnn.2016.11969.
[21] Chauhan V, Dixit P, Pandey PC. Enhancement in greenish-white photoluminescence of Zn3(VO4)2 phosphor by Bi3+ doping. Optik (Stuttg) 2021;238:166682. https://doi.org/10.1016/j.ijleo.2021.166682.
[22] Nakajima T, Isobe M, Tsuchiya T, Ueda Y, Manabe T. Correlation between luminescence quantum efficiency and structural properties of vanadate phosphors with chained, dimerized, and isolated VO 4 tetrahedra. J Phys Chem C 2010;114:5160–7. https://doi.org/10.1021/jp910884c.
[23] Nakajima TKT, Isobe M, Tsuchiya T, Ueda Y. A revisit of photoluminescence property for vanadate oxides AVO3 (A:K, Rb and Cs) and M3V2O8 (M: Mg and Zn). J Lumin 2009;129:1598–601. https://doi.org/10.1016/j.jlumin.2009.03.029.
[24] T. Nakajima, M. Isobe, T. Tsuchiya, Y. Ueda, T. Manabe, Photoluminescence property of vanadates M2V2O 7 (M: Ba, Sr and Ca), in: Opt. Mater. (Amst)., Elsevier B.V., 2010: pp. 1618–1621. https://doi.org/10.1016/j.optmat.2010.05.021.
[25] Huang Y, Yu YM, Tsuboi T, Seo HJ. Novel yellow-emitting phosphors of Ca5M4 (VO4)6 (M=Mg, Zn) with isolated VO4 tetradedra. Opt Express 2012;20:4360. https://doi.org/10.1364/oe.20.004360.
[26] Espinosa-Cerón MY, Meza-Rocha AN, Carmona-Téllez S, Chacón C, Soriano-Romero O, Lozada-Morales R. Effect of radiative energy transfer and direct excitation on the up-conversion and down-shifting emission properties of Er3+-doped Zn3(VO4)2. J Lumin 2021;238. https://doi.org/10.1016/j.jlumin.2021.118239.
[27] Qian T, Fan B, Wang H, Zhu S. Structure and luminescence properties of Zn3V2O8 yellow phosphor for white light emitting diodes. Chem Phys Lett 2019;715:34–9. https://doi.org/10.1016/j.cplett.2018.11.022.
[28] Li T, Luo J, Honda Z, Fukuda T, Kamata N. Sintering condition and optical properties of Zn3V2O8 phosphor. Adv Mater Phys Chem 2012;02:173–7. https://doi.org/10.4236/ampc.2012.23026.

[29] Luitel HN, Chand R, Torikai T, Yada M, Watari T. Rare earth free Zn3V2O8 phosphor with controlled microstructure and its photocatalytic activity. Int J Photoenergy 2013;2013:2–11. https://doi.org/10.1155/2013/410613.
[30] S. Ni, X. Wang, G. Zhou, F. Yang, J. Wang, D. He, Crystallized Zn 3 (VO4)2: Synthesis, characterization and optical property, 491 (2010) 378–381. https://doi.org/10.1016/j.jallcom.2009.10.188.
[31] Monika RS, Yadav A, Bahadur SB. Rai, Concentration and pump power-mediated color tunability, optical heating and temperature sensing via TCLs of red emission in an Er3+/Yb3+/Li+ co-doped ZnGa2O4 phosphor. RSC Adv 2019;9:40092–108. https://doi.org/10.1039/c9ra09120c.
[32] Monika, Yadav RS, Bahadur A, Rai SB. Near-infrared light excited highly pure green upconversion photoluminescence and intrinsic optical bistability sensing in a Ho3+/Yb3+ Co-Doped ZnGa2O4 Phosphor through Li+ Doping. J Phys Chem C 2020;124:10117–28. https://doi.org/10.1021/acs.jpcc.0c01554.
[33] Cao R, Peng D, Xu H, Luo Z, Ao H, Guo S, et al. Synthesis and luminescence properties of Sr3(VO4)2:Eu3+ phosphor and emission enhancement by co-doping Li+ ion. Optik (Stuttg) 2016;127:7896–901. https://doi.org/10.1016/j.ijleo.2016.05.157.
[34] Singh AK, Singh SK, Rai SB. Role of Li + ion in the luminescence enhancement of lanthanide ions: favorable modi fi cations in host matrices. RSC Adv 2014;4:27039–61. https://doi.org/10.1039/c4ra01055h.
[35] Rodríguez-Carvajal J. Recent advances in magnetic structure determination by neutron powder diffraction. Phys B Phys Condens Matter 1993;192:55–69. https://doi.org/10.1016/0921-4526(93)90108-I.
[36] Zhang LX, Li GN, Yin YY, Xing Y, Xu H, Chen JJ, et al. Zn3(VO4)2-decoration induced acetone sensing improvement of defective ZnO nanosheet spheres. Sensors Actuators, B Chem 2020;325:128805. https://doi.org/10.1016/j.snb.2020.128805.
[37] Rao Bandi V, Grandhe BK, Jayasimhadri M, Jang K, Lee HS, Yi SS, et al. Photoluminescence and structural properties of Ca3Y(VO4)3:RE3 (=Sm3, Ho3 and Tm3) powder phosphors for tri-colors. J Cryst Growth 2011;326:120–3. https://doi.org/10.1016/j.jcrysgro.2011.01.075.
[38] Lv Y, Zhang Y, Shi L, Shi JW, Li J, Li Z, et al. Role of oxygen vacancy in rare-earth-free LiCa3Mg(VO4)3 phosphor: enhancing photoluminescence by heat-treatment in oxygen flow. J Mater Sci Technol 2021;79:123–32. https://doi.org/10.1016/j.jmst.2020.11.039.
[39] Kumar P, Chauhan V, Joshi AG, Pandey PC. Optical and magnetic properties of terbium doped zinc oxide nanoparticles with lithium as charge compensator. Optik (Stuttg) 2020;216:164839. https://doi.org/10.1016/j.ijleo.2020.164839.
[40] D. Briggs, X-ray photoelectron spectroscopy (XPS), Handb. Adhes. Second Ed. (2005) 621–622. https://doi.org/10.1002/0470014229.ch22.
[41] Zhang D, Du C, Chen J, Shi Q, Wang Q, Li S, et al. Improvement of structural and optical properties of ZnAl2O4:Cr3+ ceramics with surface modification by using various concentrations of zinc acetate. J Sol-Gel Sci Technol 2018;88:422–9. https://doi.org/10.1007/s10971-018-4820-x.
[42] Wood DL, Tauc J. Weak absorption tails in amorphous semiconductors. Phys Rev B 1972;5:3144. https://doi.org/10.1103/PhysRevB.5.3144.
[43] Chauhan V, Dixit P, Pandey PC. Bi3+ assisted luminescence in SrMoO4:Sm3+ red phosphor. J Rare Earths 2021;39:1336–43. https://doi.org/10.1016/j.jre.2020.10.014.
[44] Pattnaik S, Rai VK. Impact of charge compensation on optical and thermometric behaviour of titanate phosphors. Mater Res Bull 2020;125:110761. https://doi.org/10.1016/j.materresbull.2019.110761.
[45] Ronde H, Blasse G. The nature of the electronic transitions of the vanadate group. J Inorg Nucl Chem 1978;40:215–9. https://doi.org/10.1016/0022-1902(78)80113-4.
[46] Pavitra E, Raju GSR, Park JY, Wang L, Moon BK, Yu JS. Novel rare-earth-free yellow Ca 5 Zn 3.92 in 0.08 (V 0.99 Ta 0.01 O 4) 6 phosphors for dazzling white light-emitting diodes. Sci Rep 2015;5:1–13. https://doi.org/10.1038/srep10296.
[47] Xie H, Tsuboi T, Huang W, Huang Y, Qin L, Seo HJ. Luminescence and quantum efficiencies of Eu3+-doped vanadate garnets. J Am Ceram Soc 2014;97:1434–41. https://doi.org/10.1111/jace.12771.
[48] Gao Z, Hao Y, Zheng M, Chen Y. A fluorescent dye with large Stokes shift and high stability: synthesis and application to live cell imaging. RSC Adv 2017;7:7604–9. https://doi.org/10.1039/c6ra27547h.
[49] Upasani M. Synthesis of Y3Al5O12: Eu and Y3Al5O12:Eu, Si phosphors by combustion method: comparative investigations on the structural and spectral properties. J Adv Ceram 2016;5:344–55. https://doi.org/10.1007/s40145-016-0208-y.
[50] Yadav RS, Rai SB. Effect of annealing and excitation wavelength on the downconversion photoluminescence of Sm3+ doped Y2O3 nano-crystalline phosphor. Opt Laser Technol 2019;111:169–75. https://doi.org/10.1016/j.optlastec.2018.09.049.
[51] Vishwakarma PK, Bahadur A, Maurya A, Rai SB. Large enhancement in upconverted green emission intensity from Ho3+/Yb3+ co-doped Y2Ti2O7 phosphor in the presence of Zn 2+. Mater Res Bull 2019;115:219–26. https://doi.org/10.1016/j.materresbull.2019.03.029.
[52] Meetei SD, Dorendrajit S. Effects of crystal size, structure and quenching on the photoluminescence emission intensity, lifetime and quantum yield of ZrO2: Eu3þ nanocrystals. J Lumin 2014;147:328–35. https://doi.org/10.1016/j.jlumin.2013.11.064.
[53] Singh V, Seshadri M, Pathak MS, Singh N. Sm 3+ doped calcium orthovanadate Ca 3 (VO 4) 2 – a spectral study. Spectrochim Acta – Part A Mol Biomol Spectrosc 2019;217:315–21. https://doi.org/10.1016/j.saa.2019.03.041.
[54] Dang P, Liu D, Wei Y, Li G, Lian H, Shang M, et al. Highly efficient cyan-green emission in self-activated Rb3RV2O8 (R = Y, Lu) vanadate phosphors for full-spectrum white light-emitting diodes (LEDs). Inorg Chem 2020;59:6026–38. https://doi.org/10.1021/acs.inorgchem.0c00015.
[55] Hasegawa T, Abe Y, Koizumi A, Ueda T, Toda K, Sato M. Bluish-white luminescence in rare-earth-free vanadate garnet phosphors: structural characterization of LiCa3MV3O12 (M = Zn and Mg). Inorg Chem 2018;57:857–66. https://doi.org/10.1021/acs.inorgchem.7b02820.
[56] Zhang X, Zhu Z, Guo Z, Sun Z, Zhou L, Chao Wu Z. Synthesis, structure and luminescent properties of Eu3+ doped Ca3LiMgV3O12 color-tunable phosphor. Ceram Int 2018;44:16514–21. https://doi.org/10.1016/j.ceramint.2018.06.069.